Numerical implementation of the Cubic Galileon model in PINOCCHIO

Yanling Song [ORCID],[1] Chiara Moretti [ORCID],[2,3] Pierluigi Monaco[3,4,5,6] and Bin Hu [ORCID][1]★

[1]*Department of Astronomy, Beijing Normal University, Beijing 100875, China*
[2]*Astronomy Unit, School of Physics and Astronomy, Queen Mary University of London, Mile End Road, London E1 4NS, UK*
[3]*INAF – Osservatorio Astronomico di Trieste, Via Tiepolo 11, I-34143 Trieste, Italy*
[4]*Dipartimento di Fisica dell'Universitá di Trieste, Sezione di Astronomia, via Tiepolo 11, I-34143 Trieste, Italy*
[5]*IFPU – Institute for Fundamental Physics of the Universe, Via Beirut 2, I-34014 Trieste, Italy*
[6]*INFN – Sezione di Trieste, 34127 Trieste, Italy*

ABSTRACT
We present a perturbative treatment of non-linear galaxy clustering in the context of the cubic Galileon modified gravity model, in terms of second-order Lagrangian Perturbation theory and an extension of ellipsoidal collapse that includes Vainshtein screening. We numerically implement such prescriptions in the approximate PINOCCHIO code, and use it to generate realizations of the matter density field and halo catalogues with different prescriptions for ellipsoidal collapse. We investigate the impact of three different approximations in the computation of collapse times on the halo mass function, halo bias, and matter power spectrum. In the halo mass function, both the modified gravity effect and the screening effect are significant in the high-mass end, similar to what is found for other MG models. We perform a comparison with *N*-body simulations to assess the validity of our approach, and show that we can reproduce the same trend observed in simulations for all quantities considered. With a simple modification to the grouping algorithm of PINOCCHIO to take into account the gravity modification, and without the need to re-calibrate the algorithm, we show that we can reproduce the linear halo bias and the mildly non-linear matter power spectrum of simulations with good accuracy, especially for the implementation with Vainshtein screening. We stress that, while approximate, our method is orders of magnitude faster than a full *N*-body simulation, making it an optimal tool for the quick generation of large sets of halo catalogues for cosmological observables.

Key words: Galaxy: halo – dark energy – large-scale structure of Universe.

1 INTRODUCTION

Within the standard ΛCDM cosmological model, the observed accelerated expansion of the Universe is ascribed to the presence of dark energy (DE) in the form of a cosmological constant Λ: a perfect fluid with constant energy and equation of state, whose negative pressure $P_\Lambda = -\rho_\Lambda$ is responsible for the accelerated expansion. DE makes up most of the energy density of the Universe today together with cold dark matter (CDM), however, its nature remains elusive. In the standard framework, the cosmological constant Λ is thought to be related to vacuum energy: an interpretation that, despite the model fitting extremely well most cosmological observations (Alam et al. 2017; Aghanim et al. 2020; DES Collaboration 2021), poses severe theoretical problems (Carroll 2001). Additionally, tensions in some of the cosmological parameters as measured by early and late-time probes such as the Cosmic Microwave Background and redshift-space distortions of galaxies (Aghanim et al. 2020; DES Collaboration 2021; Heymans et al. 2021) have prompted the study of structure formation in the context of beyond-ΛCDM models. Many alternatives have been proposed, from exotic DE models to modified gravity (MG, see Bull et al. 2016; Koyama 2018; Ishak

2019 for recent reviews). While the former are mainly characterized by a dynamically evolving equation of state, the latter focus on the possibility that General Relativity (GR) is not the correct theory to describe gravity on cosmological scales, and introduce an additional fifth force that drives cosmic acceleration.

On the other hand GR has successfully passed several stringent tests, therefore any viable MG model should be able to evade such constraints and reduce to GR on small scales. In order to be consistent with both small- and large-scale observations, the additional MG fifth force has to be shielded in high density regions. This is achieved by means of a so-called screening mechanism. Screening mechanisms can be classified in three general categories (Lombriser 2016), based on the condition that the Newtonian gravitational potential Ψ_N or its derivatives exceed a certain threshold Λ_T:

(i) screening at large field values, such as the chameleon (Khoury & Weltman 2004) or symmetron (Hinterbichler & Khoury 2010) models. These are very similar to the large field inflation model: the screening effect turns on in regions where the Newtonian gravitational potential exceeds a certain threshold, $|\Psi_N| > \Lambda_T$. A high density environment plays a key role in this mechanism;

(ii) screening with first derivatives, such as in k-mouflage models (Babichev, Deffayet & Ziour 2009). This screening effect operates

★ E-mail: bhu@bnu.edu.cn

when the local gravitational acceleration is above a certain threshold, $|\nabla \Psi_N| > \Lambda_T^2$;

(iii) screening with second derivatives, such as Vainshtein screening (Vainshtein 1972). This screening mechanism activates when the local curvature is large, $|\nabla^2 \Psi_N| > \Lambda_T^3$. Unlike the chameleon mechanism, Vainshtein screening does not rely on the environment, the screening radius is jointly determined by the Schwarzschild radius of the object and the Hubble radius.

The investigation of alternatives to the standard cosmological model is indeed one of the key targets of modern cosmology. Upcoming Stage-IV galaxy surveys, such as Euclid,[1] LSST,[2] WFIRST,[3] DESI,[4] J-PAS,[5] CSST,[6] will probe the clustering of galaxies to high precision, allowing to test different MG models in the linear and mildly non-linear regime of structure formation (Amendola et al. 2013; Alam et al. 2020).

It is therefore key that accurate theoretical modelling beyond GR is prepared in advance in order to compare to observations, with a particular focus on the non-linear and mildly non-linear regimes. The most reliable tool to trace the growth of structures deep into the non-linear regime are *N*-body simulations. However, *N*-body simulations are computationally extremely expensive, in particular when they include MG.

This paper studies the modelling of non-linearities in the framework of perturbation theory (PT) in the context of the cubic Galileon model (Nicolis, Rattazzi & Trincherini 2009). In particular, we focus on a numerical implementation in the PINOCCHIO code (PINpointing Orbit-Crossing Collapsed Hierarchical Objects; Monaco, Theuns & Taffoni 2002a; Monaco et al. 2002b, 2013; Taffoni, Monaco & Theuns 2002; Munari et al. 2017), an algorithm to quickly generate simulated dark matter halo catalogues based on Lagrangian PT and ellipsoidal collapse.

We organize the papers as follows: in Section 2 we describe the background, linear and non-linear perturbation evolution of the cubic Galileon model. In Section 3, we present the first- and second-order Lagrangian PT for the cubic Galileon model. In Section 4, we give the prescription of the 'G3-PINOCCHIO' algorithm, including the extension of ellipsoidal collapse. In Section 5, we show the non-linear matter power spectrum and mass function obtained with the code, as well as a prediction for the linear bias. Finally, we present our conclusions in Section 6.

2 CUBIC GALILEON

Galileon gravity (Nicolis et al. 2009) is proposed in the inspiration of flat space quantum field theories. The latter are invariant under the transformation $\phi \rightarrow \phi + b_\mu x^\mu + c$, where b_μ and c are a constant vector and scalar in flat space, respectively. The existence of b_μ and c indicates, respectively, the Galilean and shift symmetry. To avoid the Ostrogradski instability, the field equation includes up to second-order time derivatives. When extending to curved space–time, the non-minimal coupling between the Galileon field and the metric breaks the Galilean symmetry, but keeps the shift symmetry preserved. Such model, called covariant Galileon model,

has a Lagrangian of the form

$$
S = \int d^4x \sqrt{-g} \left\{ \frac{M_{pl}^2}{2} R - \frac{1}{2} c_2 X + \frac{c_3}{M^3} X \Box \phi + \frac{c_4}{4M^6} X^2 R \right.
$$
$$
- \frac{c_4}{M^6} X[(\Box\phi)^2 - \phi^{;\mu\nu}\phi_{;\mu\nu}] + \frac{3c_5}{4M^9} X^2 G_{\mu\nu} \phi^{;\mu\nu}
$$
$$
\left. + \frac{c_5}{2M^9} X[(\Box\phi)^3 - 3\Box\phi\phi_{;\mu\nu}\phi^{;\mu\nu} + 2\phi^{;\mu\nu}\phi_{;\mu\sigma}\phi_{;\nu}^{;\sigma}] \right\}, \tag{1}
$$

where M_{pl} is the Planck mass $M_{pl}^{-2} = 8\pi G$, g, R, $G_{\mu\nu}$ are, respectively, the determinant of the metric, the Ricci scalar and the Einstein tensor, c_2, c_3, c_4, c_5 are dimensionless constants and $M^3 = M_{pl} H_0^2$, with H_0 the present Hubble parameter. $X = \phi_{;\mu} \phi^{;\mu}$ is the kinetic term of the scalar field. The semicolon in equation (1) represents the covariant derivative. There are three branches of covariant Galileon: the G3 branch, known as cubic Galileon, with $c_3 \neq 0$, $c_4 = c_5 = 0$, the G4 branch, also called quartic Galileon, with c_3, $c_4 \neq 0$, $c_5 = 0$ and the G5 branch, also known as quintic Galileon, with c_3, c_4, $c_5 \neq 0$. Some recent studies that focus on constraining the covariant Galileon model by means of various cosmological observations include Barreira et al. (2012, 2013b, 2014b), Neveu et al. (2013), Peirone et al. (2018), Renk et al. (2017), and Frusciante et al. (2020). Although this model is disfavoured by current CMB and galaxy clustering data, its extension can fit current cosmological observations (Peirone et al. 2019; Frusciante et al. 2020).

The breakthrough discovery of gravitational waves (GW) from the merger of a neutron star binary (Abbott et al. 2017a) by the LIGO and Virgo collaborations puts a tight constraint on the GW speed (Abbott et al. 2017b), effectively ruling out several MG models. In particular, the G4 and G5 branches are ruled out (Baker et al. 2017; Creminelli & Vernizzi 2017; Ezquiaga & Zumalacárregui 2017) with a high confidence level. In the G3 branch, however, the scalar field is minimally coupled to gravity, and the GW speed is unaltered. Hence, G3 is still a viable MG model even according to GW constraints.

An additional reason to investigate the cubic Galileon model is related to the screening mechanism it features. Since the G3 field drives cosmic acceleration via the non-canonical kinetic energy, the extra gravitational force is screened via the Vainshtein mechanism. While chameleon screening has been extensively discussed during the past decades, in particular in the context of $f(R)$ gravity (e.g. Li et al. 2012; Puchwein, Baldi & Springel 2013; Llinares, Mota & Winther 2014), Vainshtein screening is usually studied as feature of nDGP modified gravity (e.g. Barreira, Bose & Li 2015; Winther et al. 2015, 2017; Hernández-Aguayo et al. 2021). Studies of this type of screening mechanism that focus on cubic Galileon are instead more rare; some examples include the work of Schmidt (2009), Barreira et al. (2013a), and Li, Zhao & Koyama (2013).

A first step to include MG in the PINOCCHIO code focused indeed on $f(R)$ gravity, which features scale-dependent growth and chameleon screening (Moretti et al. 2020). In this work, we present an implementation of scale-independent MG models with Vainshtein screening, focusing in particular on the G3 model, and study its performance with PINOCCHIO.

2.1 Background evolution under cubic Galileon

The Einstein equation and the scalar field equation can be obtained by varying the action with respect to the metric and scalar field, respectively. In the spatially flat Friedmann–Lemaître–Robertson–Walker (FLRW) metric, one can get the first- and second-Friedmann equations

$$
3H^2 = \kappa(\bar\rho_m + \bar\rho_r + \bar\rho_\phi), \tag{2}
$$

$$0 = 3\dot{H} + 3H^2 + \frac{\kappa}{2}\left[\bar{\rho}_m + \bar{\rho}_r + \bar{\rho}_\phi + 3(\bar{P}_\phi + \bar{P}_r)\right] \,, \tag{3}$$

where $\kappa = 8\pi G$, $\bar{P}_r = \frac{1}{3}\bar{\rho}_r$. Quantities with a bar are background quantities and the over dot represents the time derivative. The expressions for $\bar{P}_\phi$, $\bar{\rho}_\phi$ are

$$\bar{P}_\phi = \frac{1}{2}c_2\dot{\bar{\phi}}^2 - 2\frac{c_3}{M^3}\dot{\bar{\phi}}^2\ddot{\bar{\phi}} \,, \tag{4}$$

$$\bar{\rho}_\phi = \frac{1}{2}c_2\dot{\bar{\phi}}^2 + 6\frac{c_3}{M^3}H\dot{\bar{\phi}}^3. \tag{5}$$

The matter component satisfies the continuity equation $\dot{\bar{\rho}}_m + 3H\bar{\rho}_m = 0$, the radiation component satisfies $\dot{\bar{\rho}}_r + 4H\bar{\rho}_r = 0$, and the scalar field component (or the DE component) satisfies $\dot{\bar{\rho}}_\phi + 3H(\bar{\rho}_\phi + \bar{P}_\phi) = 0$. For the scalar field, we use the tracker solution of De Felice & Tsujikawa (2010):

$$\dot{\bar{\phi}} = \xi H_0^2/H \,. \tag{6}$$

The meaning of tracker denotes that different initial conditions of the background Galileon field give rise to different time evolution that eventually merge into a common trajectory. Here $\bar{\phi}$ is the background field, H is the Hubble parameter, and ξ is a dimensionless constant. Equation (6) express the solution of the background scalar field in terms of the Hubble parameter. Naively, it would seem that there are three extra parameters in the G3 model compared with ΛCDM, namely $\{c_2, c_3, \xi\}$. However, that is not the case: in what follows we show that the number of parameters in G3 is actually the same as those in ΛCDM. By substituting the tracker solution equation (6) into the 1st-Friedmann equation, one can get

$$E^4 = (\Omega_{m,0}a^{-3} + \Omega_{r,0}a^{-4})E^2 + \frac{1}{6}c_2\xi^2 + 2c_3\xi^3 \,, \tag{7}$$

where E is the dimensionless Hubble parameter $E = H/H_0$, $\Omega_{m,0} = \bar{\rho}_{m,0}/(3M_{pl}^2H_0^2)$, and $\Omega_{r,0} = \bar{\rho}_{r,0}/(3M_{pl}^2H_0^2)$ are the present matter density and radiation density, respectively, and a is the scale factor. Defining

$$\Omega_{\Lambda,0} = 1 - \Omega_{m,0} - \Omega_{r,0} = \frac{1}{6}c_2\xi^2 + 2c_3\xi^3 \,, \tag{8}$$

we can get a parametrized Hubble parameter

$$H = H_0\sqrt{\frac{\Omega_{m,0}a^{-3} + \Omega_{r,0}a^{-4} + \sqrt{(\Omega_{m,0}a^{-3} + \Omega_{r,0}a^{-4})^2 + 4\Omega_{\Lambda,0}}}{2}}. \tag{9}$$

To avoid the scaling degeneracy and without loss of generality (Barreira et al. 2014b), one can assume $c_2 = -1$. Combining the scalar field equation and the tracker solution, we can get a constraining equation on the G3 parameters:

$$c_2\xi + 6c_3\xi^2 = 0 \,. \tag{10}$$

From equations (8) and (10), we have

$$c_3 = \frac{1}{6\sqrt{6\Omega_{\Lambda,0}}}, \quad \xi = \sqrt{6\Omega_{\Lambda,0}} \,. \tag{11}$$

One can see that, once $\Omega_{\Lambda,0}$ is given, all the G3 model parameters are fixed and there are no additional parameters with respect to ΛCDM. Through the 2nd-Friedmann equation, we obtain the acceleration parameter

$$\dot{H} = \frac{\frac{H_0^4}{H^2}\Omega_{\Lambda,0} - H^2 - \frac{1}{2}H_0^2(\Omega_{m,0}a^{-3} + 2\Omega_{r,0}a^{-4})}{1 + \frac{H_0^4}{H^4}\Omega_{\Lambda,0}} \,. \tag{12}$$
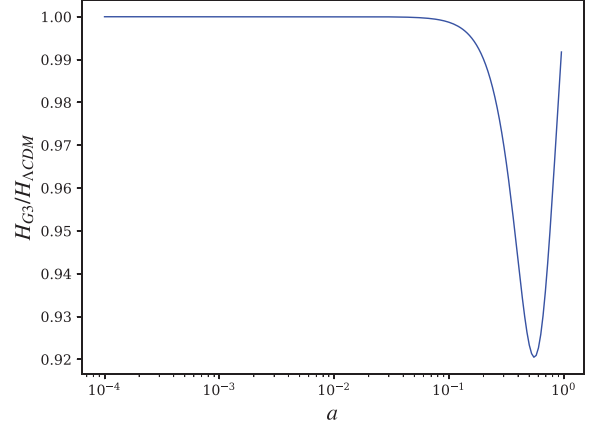
Figure 1. Ratio of the Hubble parameter in G3 and the ΛCDM model as a function of the scale factor a.

The above equations fully describe the background cosmology in the G3 model. Fig. 1 shows the ratio of the Hubble parameter between G3 and ΛCDM as a function of the scale factor a: one can see that the two are the same at early times. Starting from $a \simeq 0.1$, the ratio decreases, reaches a minimum around $a \simeq 0.5$, then bounces back and approaches unity at present time.

2.2 Linear perturbations in cubic Galileon

In the context of linear perturbation theory and in the framework of GR, the matter anisotropic stress can be ignored. The Weyl potential $\Phi_+ = (\Phi + \Psi)/2$ felt by relativistic particles is equal to the Newtonian potential Ψ felt by non-relativistic particles, namely $\Phi_+ = \Phi = \Psi$. Here, we denote the Newtonian potential as Ψ and the spatial curvature perturbation as Φ. Generally, the equality $\Phi = \Psi$ does not hold in MG models due to the existence of the Compton wavelength of the extra scalar field: the gravitational force below and above this wavelength is different. This phenomenon can be parametrized in the 00 component of the Einstein equation by means of a function μ^L,[7] that in general is time- and scale-dependent:

$$k^2\Psi = -4\pi G\mu^L(a, k)a^2\bar{\rho}_m\Delta \,, \tag{13}$$

where $\Delta = \delta + 3aHv/k$, with $\delta = \delta\rho_m/\bar{\rho}_m$ the matter density contrast in the Newtonian conformal gauge, and v the irrotational part of the peculiar velocity. One can read the μ^L function as the ratio between the effective gravitational coupling G_{eff} and the Newton constant G_N, with the superscript 'L' denoting linear level. In general, chameleon models feature a k-dependent μ^L function, which translates in scale-dependent growth even at linear level. For the k-essence type of MG models, however, cosmic acceleration is driven by the non-canonical kinetic energy, the scalar field is effectively massless and the corresponding Compton wavelength is on or above the Hubble horizon scale. The effective gravitational coupling at linear level may not be equal to the Newton constant, but it is constant on all the scales relevant to the linear regime (Peirone et al. 2018). Hence, for this type of MG models (that include the G3 model we are considering in this work), $\Phi = \Psi$ is still valid and μ^L is a function of time only.

The linear perturbation regime of MG models has been extensively studied in the past few years. In particular, it has been shown both theoretically and numerically that single field models can be re-expressed in the language of the Effective Field Theory of Dark

---

[7]We also call this μ function the *gravitational slip function*.

Energy (EFTofDE; Bloomfield et al. 2013; Gubitosi, Piazza & Vernizzi 2013; Piazza & Vernizzi 2013; Hu et al. 2014; Zumalacárregui et al. 2017; Frusciante & Perenon 2020). The action in the EFTofDE reads

$$S = \int d^4x \sqrt{-g} \left\{ \frac{M_{\rm pl}^2}{2} \Omega(t) R + \Lambda(t) - c(t)\delta g^{00} \right.$$
$$+ \frac{M_2^4(t)}{2}(\delta g^{00})^2 - \frac{\bar{M}_1^3(t)}{2}\delta g^{00}\delta K_\mu^\mu - \frac{\bar{M}_2^2(t)}{2}(\delta K_\mu^\mu)^2$$
$$- \frac{\bar{M}_3^2(t)}{2}\delta K_j^i \delta K_i^j + \frac{\hat{M}^2(t)}{2}\delta g^{00}\delta R^{(3)}$$
$$\left. + m_2^2(t)(g^{\mu\nu} + n^\mu n^\nu)\partial_\mu(g^{00})\partial_\nu(g^{00}) \right\} + S_{\rm m}[g_{\mu\nu}, \chi_i], \quad (14)$$

where δg_{00}, $\delta K_{\mu\nu}$, δK, and $\delta R^{(3)}$ are perturbations of the time–time component of the metric, the external curvature and its trace, and the 3D Ricci scalar in the constant time hypersurface, $S_{\rm m}$ is the minimally coupled term for all matter fields χ_i with metric $g_{\mu\nu}$, and M_i, $\bar{M}_i$, and $\hat{M}_i$ are the EFT functions. The perturbation of the scalar field can be expressed by the infinitesimal time diffeomorphism, $t \rightarrow t + \pi(x^\mu)$, where π is the perturbation of the scalar field.

Following Pogosian & Silvestri (2016), we combine the Einstein equation and the scalar field equation under the quasi-static approximation, which applies only to scales below the sound horizon of the scalar field. Under this approximation, we ignore the time derivatives of the gravitational potential and the scalar field. One can then derive the following expression for $\mu^{\rm L}(a, k)$ in the EFTofDE framework:

$$\frac{\mu^{\rm L}}{2M_{\rm pl}^2} = \frac{f_1 + f_2 a^2/k^2}{f_3 + f_4 a^2/k^2}, \quad (15)$$

with

$$f_1 = c - \frac{1}{2}(H + \partial_t)\bar{M}_1^3,$$
$$f_2 = -3c\dot{H} + \frac{3}{2}(3H\dot{H} + \dot{H}\partial_t + \ddot{H})\bar{M}_1^3,$$
$$f_3 = 2M_{\rm pl}^2\Omega f_1 - \frac{1}{2}\bar{M}_1^6,$$
$$f_4 = 2M_{\rm pl}^2\Omega f_2. \quad (16)$$

In the upper panel of Fig. 2, we show the linear part of the μ function as a function of redshift z and wavenumber k. The values are encoded in the colour bar. On top of that, we show contours with constant $\mu^{\rm L}$ values. One can see that the contours are vertically distributed, in line with the fact that the modification of the gravitational force is scale independent. Furthermore, the μ values are significantly larger at low redshifts: the gravity enhancement reaches a value of around 2 at present time, while it approaches unity for redshifts $z > 1$. In the lower panel of Fig. 2 we show the nonlinear $\mu^{\rm NL}$ function that includes Vainshtein screening, discussed in the next section, as a function of both redshift z (horizontal axis) and the local density contrast δ (vertical axis). One can see that with higher local density, the extra gravitational force is shielded for all redshifts considered.

2.3 Nonlinear clustering in cubic Galileon

We now consider the second-order perturbation contribution. Under the quasi-static approximation, after ignoring the terms suppressed by the time derivatives and Hubble expansion, the 00 component of the Einstein equation reads (Frusciante & Pace 2020)

$$\frac{\partial^2 \Phi}{a^2} = 4\pi G \bar{\rho}_{\rm m}\delta_{\rm m} - 8\pi G \frac{c_3}{M^3}\dot{\phi}^2 \frac{\partial^2(\delta\phi)}{a^2}, \quad (17)$$
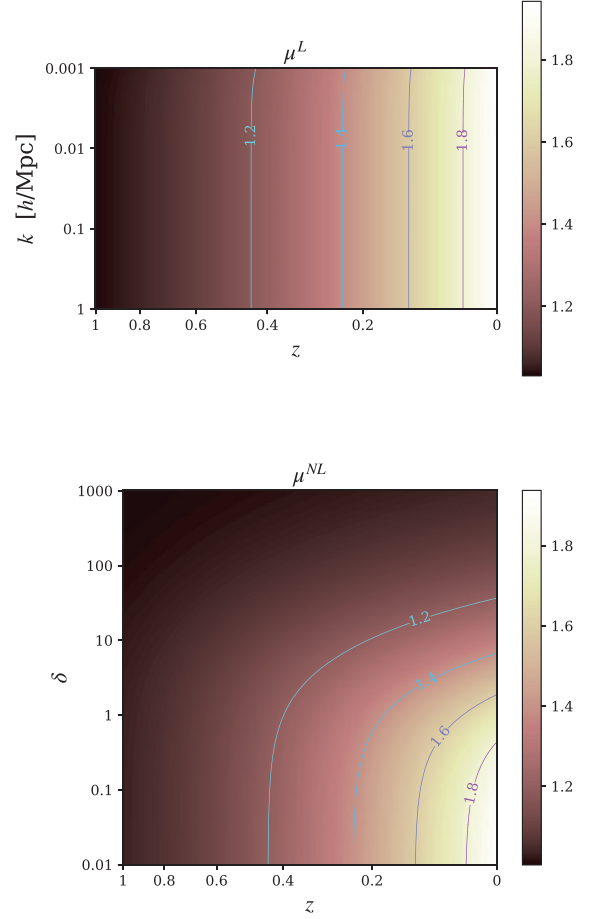

Figure 2. 2D contour plot of the μ function. The upper panel shows the linear part $\mu^{\rm L}$ as a function of redshift z (horizontal axis) and wavenumber k (vertical axis), with lines showing the isocontours. The lower panel shows the same quantity but including Vainshtein screening $\mu^{\rm NL}$ (equation 25), again as a function of redshift z (horizontal axis), but with the local matter density contrast δ on the vertical axis. Values different from 1 mark a deviation from GR.

where ∂ denotes derivatives with respect to comoving spatial coordinates. The equation for the scalar field is

$$-\frac{c_3}{M^3}\dot{\phi}^2\frac{\partial^2\Psi}{a^2} = \left[\frac{1}{2}c_2 + 2\frac{c_3}{M^3}(\ddot{\phi} + 2H\dot{\phi})\right]\frac{\partial^2\delta\phi}{a^2}$$
$$+ \frac{c_3}{M^3}\left[(\frac{\partial^2\delta\phi}{a^2})^2 - (\frac{\partial_i\partial_j\delta\phi}{a^2})^2\right]. \quad (18)$$

Since $\Psi = \Phi$ is valid in both the linear and non-linear regime, combining equations (17) and (18) one gets

$$\frac{\partial^2(\delta\phi)}{a^2} + \lambda^2(a)\left[(\frac{\partial^2(\delta\phi)}{a^2})^2 - (\frac{\partial_i\partial_j(\delta\phi)}{a^2})^2\right]$$
$$= -4\pi G \zeta(a)\bar{\rho}_{\rm m}\delta_{\rm m}, \quad (19)$$

where

$$\lambda^2(a) = \frac{c_3/M^3}{\frac{1}{2}c_2 + 2\frac{c_3}{M^3}(\ddot{\phi} + 2H\dot{\phi}) - 8\pi G(\frac{c_3}{M^3})^2\dot{\phi}^4}, \quad \zeta(a) = \lambda^2\dot{\phi}^2.$$

Assuming a spherically symmetric profile for $\delta\phi$, equation (19) becomes

$$\frac{1}{r^2}\frac{d}{dr}\left(r^2\frac{d\delta\phi}{dr}\right) - \frac{2\lambda^2}{r^2}\frac{d}{dr}\left[r\left(\frac{d\delta\phi}{dr}\right)^2\right] = -4\pi G \zeta \bar{\rho}_{\rm m}\delta_{\rm m}, \quad (20)$$

a second-order ordinary differential equation. After integrating once, it becomes

$$r^2 \frac{d\delta\phi}{dr} - 2\lambda^2 r \left(\frac{d\delta\phi}{dr}\right)^2 = -G\zeta m(r) , \qquad (21)$$

where $m(r) = 4\pi \int_0^r r'^2 \bar\rho_{\rm m}(r')\delta_{\rm m}(r')dr'$ is the mass enclosed in a sphere of radius r. Considering a top-hat density profile with radius R, when $r \leq R$ the physical solution of equation (21) reads (Frusciante et al. 2020)

$$\frac{d\delta\phi}{dr} = \frac{r}{4\lambda^2}\left(1 - \sqrt{1 + \frac{r_V^3}{r^3}}\right) , \qquad (22)$$

where r_V is the Vainshtein radius of the enclosed mass, given by

$$r_V^3 = 8Gm(r)\lambda^2\zeta . \qquad (23)$$

From equation (22) one can see that $d\delta\phi/dr \propto r$ for $r \leq R$, so that $\partial^2(\delta\phi)$ is constant within radius R. Taking the derivative of equation (22) and substituting it in equation (17), we get the modified Poisson equation

$$\frac{\partial^2\Psi}{a^2} = 4\pi G\mu^{\rm NL}(a, R)\bar\rho_{\rm m}\delta_{\rm m} , \qquad (24)$$

where $\mu^{\rm NL}(a, R)$ includes the non-linear contribution which is constant within the Top Hat

$$\mu^{\rm NL}(a, R) = 1 + 2(\mu^{\rm L} - 1)\left(\frac{R}{R_V}\right)^3\left(\sqrt{1 + \frac{R_V^3}{R^3}} - 1\right). \qquad (25)$$

In the above equation, $\mu^{\rm L} = 1 + 8\pi G\frac{c_3}{M^3}\dot\phi^2\zeta(a)$ is the linear part of the μ function. R_V is the Vainshtein radius of the enclosed mass with a top-hat density profile $R_V^3 = 8Gm(R)\lambda^2\zeta \propto R^3$. Then, one can write

$$\left(\frac{R}{R_V}\right)^3 = \frac{1}{4\Omega_{\rm m}H^2\lambda^2\zeta}\frac{1}{\delta_{\rm m}}. \qquad (26)$$

When the density perturbation is large such that $R \ll R_V$, $\mu^{\rm NL} \to 1$ recovering GR, while for small perturbations when $R \gg R_V$, $\mu^{\rm NL} \to \mu^{\rm L}$, recovering the linear result. In the lower panel of Fig. 2, we plot $\mu^{\rm NL}$ as a function of redshift z and the top-hat object density δ. One can see that for low redshifts $z < 1$, it deviates from GR, same as the linear $\mu^{\rm L}$ function. When the density contrast is about 0.01–0.1, $\mu^{\rm NL}$ is similar to $\mu^{\rm L}$, roughly depending on time only. For large values of $\delta > 1000$, $\mu^{\rm NL} \to 1$, recovering GR. At fixed redshift, the value of $\mu^{\rm NL}$ for a high density contrast is smaller than that of a low density contrast.

3 LAGRANGIAN PERTURBATION THEORY FOR CUBIC GALILEON

In this section, we briefly review the linear and second-order Lagrangian perturbation theory (LPT) for the G3 model (Song & Hu 2021). The equation of motion for the displacement field ($\vec{S}$) in Lagrangian coordinates are

$$\nabla_x \cdot \hat{T}\vec{S} = -A(a)\delta - B(a)\left[\left(\frac{\partial^2(\delta\phi)}{a^2}\right)^2 - \left(\frac{\partial_i\partial_j(\delta\phi)}{a^2}\right)^2\right] , \qquad (27)$$

where

$$\hat{T} = \frac{d^2}{dt^2} + 2H\frac{d}{dt} , \qquad (28)$$

$$A(a) = 4\pi G\bar\rho_{\rm m}\left(1 + 8\pi G\frac{c_3}{M^3}\dot\phi^2\zeta(a)\right) , \qquad (29)$$

$$B(a) = 8\pi G\frac{c_3}{M^3}\dot\phi^2\lambda^2(a). \qquad (30)$$

Notice that the differential operation ∇_x is in Eulerian coordinates. Transforming to Lagrangian coordinates one can write

$$\nabla_x \cdot \hat{T}\vec{S} = (J^{-1})_{ij}\hat{T}S_{i,j} = (\delta_{ij} - S_{i,j})\hat{T}S_{i,j}$$
$$= \hat{T}S_{i,i} - S_{i,j}\hat{T}S_{i,j} , \qquad (31)$$

where J is the Jacobian of the coordinate transformation, and $S_{i,i}$, $S_{i,j}$ are now spatial derivatives with respect to Lagrangian coordinates. Substituting equation (31) in equation (27), we can write the displacement field equation in Lagrangian coordinates

$$\hat{T}S_{i,i} - S_{i,j}\hat{T}S_{i,j} = -A(a)\delta$$
$$- B(a)\left[\left(\frac{\partial^2(\delta\phi)}{a^2}\right)^2 - \left(\frac{\partial_i\partial_j(\delta\phi)}{a^2}\right)^2\right]. \qquad (32)$$

Expanding δ, $\delta\phi$, $\vec{S}$ with respect to a small parameter ε

$$\delta = \varepsilon\delta^{(1)} + \varepsilon^2\delta^{(2)} + ..., \qquad (33)$$

$$\vec{S} = \varepsilon\vec{S}^{(1)} + \varepsilon^2\vec{S}^{(2)} + ... \qquad (34)$$

$$\delta\phi = \varepsilon(\delta\phi)^{(1)} + \varepsilon^2(\delta\phi)^{(2)} + ..., \qquad (35)$$

one can split the above equations into serial differential equations according to their orders. At first order, the displacement field equation reads

$$(\hat{T} - A(a))S_{i,i}^{(1)}(t, \vec{q}) = 0. \qquad (36)$$

Since $(\hat{T} - A(a))$ only depends on time, $S_{i,i}^{(1)}(t, \vec{q})$ can be separated into time- and space-dependent components. Transforming the above equation to Fourier space, we obtain

$$S_{i,i}^{(1)}(\vec{k}, t) = -D_1(t)\delta^{(1)}(\vec{k}, t_0) , \qquad (37)$$

where the first-order growth factor $D_1(t)$ satisfies

$$(\hat{T} - A(a))D_1(t) = 0. \qquad (38)$$

Like in standard GR, the linear growth in G3 only has temporal dependence. For second order in PT, the displacement field equation reads

$$\hat{T}S_{i,i}^{(2)}(\vec{k}, t) - [S_{i,j}^{(1)}\hat{T}S_{i,j}^{(1)}](\vec{k}, t) =$$
$$-A(a)\delta^{(2)}(\vec{k}, t) - B(a)\left[\left(\frac{\partial^2(\delta\phi)^{(1)}}{a^2}\right)^2 - \left(\frac{\partial_i\partial_j(\delta\phi)^{(1)}}{a^2}\right)^2\right](\vec{k}, t). \qquad (39)$$

Through equation (19) we obtain

$$\frac{k^2}{a^2}(\delta\phi)^{(1)}(\vec{k}, t) = 4\pi G\zeta(a)\bar\rho_{\rm m}D_1(t)\delta^{(1)}(\vec{k}, t_0). \qquad (40)$$

Plugging equation (40), (37) into equation (39), we can write

$$[\hat{T} - A(a)]S_{i,i}^{(2)}(\vec{k}, t) = -\left[\frac{1}{2}A(a) + B(a)(4\pi G\bar\rho_{\rm m}\zeta(a))^2\right]$$
$$\times \int_{\vec{k}_{12}=\vec{k}}\left[1 - \frac{(\vec{k}_1 \cdot \vec{k}_2)^2}{k_1^2k_2^2}\right]D_1^2(t)\delta_{k_1}^{(1)}(t_0)\delta_{k_2}^{(1)}(t_0)$$
$$= -C(a)\int_{\vec{k}_{12}=\vec{k}}\left[1 - \frac{(\vec{k}_1 \cdot \vec{k}_2)^2}{k_1^2k_2^2}\right]D_1^2(t)\delta_{k_1}^{(1)}(t_0)\delta_{k_2}^{(1)}(t_0), \qquad (41)$$

where $\int_{\vec{k}_{12}=\vec{k}}$ is short-hand notation for $\int \frac{d^3\vec{k}_1 d^3\vec{k}_2}{(2\pi)^3}\delta(\vec{k} - \vec{k}_1 - \vec{k}_2)$, and

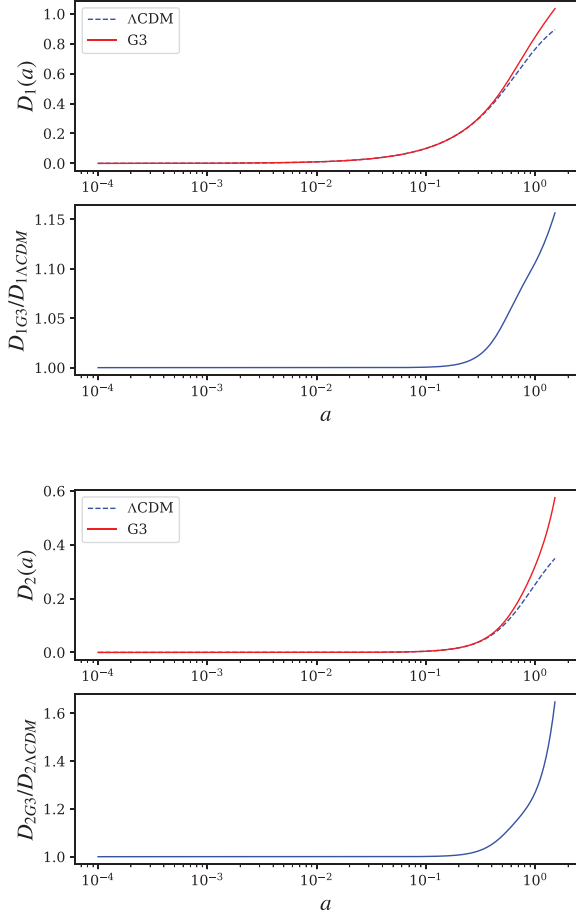$$C(a) = \frac{1}{2}A(a) + B(a)(4\pi G\bar\rho_{\rm m}\zeta(a))^2.$$

Figure 3. The linear (top panel) and second-order (third panel) growth factors as a function of the scale factor a. Dashed blue lines are ΛCDM quantities, while solid red lines are G3 quantities. The second and bottom panels show, respectively, the ratio of the G3 linear and second-order growth functions to their ΛCDM counterparts.

The second-order displacement field then reads

$$S_{i,i}^{(2)}(\vec{k}, t) = \int_{\vec{k}_{12}=\vec{k}} \widetilde{D}_2(\vec{k}_1, \vec{k}_2, t) D_1^2(t) \delta_{k_1}^{(1)}(t_0) \delta_{k_2}^{(1)}(t_0), \quad (42)$$

where $\widetilde{D}_2(\vec{k}_1, \vec{k}_2, t)$ is a normalized second-order growth factor that satisfies

$$[\hat{T} - A(a)]\widetilde{D}_2(\vec{k}_1, \vec{k}_2, t) = -C(a)\left[1 - \frac{(\vec{k}_1 \cdot \vec{k}_2)^2}{k_1^2 k_2^2}\right]. \quad (43)$$

Since $[\hat{T} - A(a)]$ depends only on time, $\widetilde{D}_2(\vec{k}_1, \vec{k}_2, t)$ can also be separated into the product of time component $\widetilde{D}_2(t)$ and space component $[1 - \frac{(\vec{k}_1 \cdot \vec{k}_2)^2}{k_1^2 k_2^2}]$. Thus equation (42) can be rewritten as

$$S_{i,i}^{(2)}(\vec{k}, t) = D_1^2(t)\widetilde{D}_2(t) \int_{\vec{k}_{12}=\vec{k}} \left[1 - \frac{(\vec{k}_1 \cdot \vec{k}_2)^2}{k_1^2 k_2^2}\right] \delta_{k_1}^{(1)}(t_0) \delta_{k_2}^{(1)}(t_0) . \quad (44)$$

Redefining $-2D_1^2(t)\widetilde{D}_2(t)$ as $D_2(t)$, then the second-order growth factor $D_2(t)$ satisfies

$$[\hat{T} - A(a)]D_2(t) = 2C(a)D_1^2(t) . \quad (45)$$

Again, D_2 is independent of k, as it is in the standard GR case. To get the second-order displacement field $S_{i,i}^{(2)}(\vec{k}, t)$, one just needs to convolv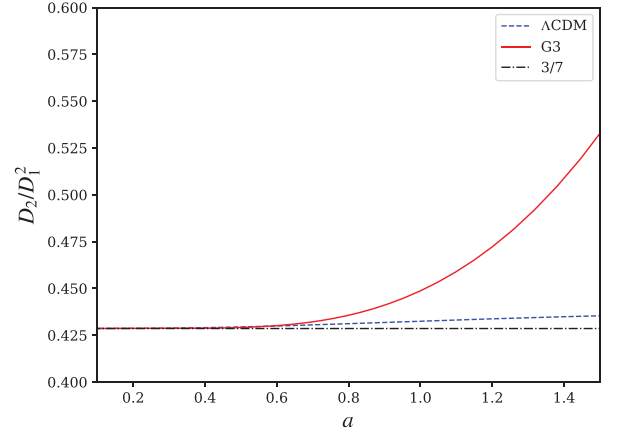e the initial linear density fields with a kernel as in equation (44). The difference between G3 and ΛCDM lays in the temporal evolution of the linear and second-order growth factors. When $A(a) = 4\pi G \bar{\rho}_m$, $B(a) = 0$, $C(a) = 2\pi G \bar{\rho}_m$, the equations for the first- and second-order displacements recover ΛCDM (Song & Hu 2021).

We choose the initial conditions for the D_1 differential equation to match an Einstein–de Sitter universe, i.e. $D_1(a) = a$, $\frac{dD_1}{da} = 1$. In the top panel of Fig. 3, we show $D_1(a)$ in G3 (red solid line) and ΛCDM (blue dashed line), with their ratio in the second panel, as a function of the scale factor a. One can see that D_1 in G3 is the same as in ΛCDM at early times. Starting from $a \simeq 0.2$, D_1 in G3 increases faster than in ΛCDM, with their ratio reaching ~ 15 per cent at present times. The initial conditions for D_2 are assumed to be $D_2(a) = \frac{3}{7}a^2$, $\frac{dD_2}{da} = \frac{6}{7}a$, corresponding to matter domination. In the third panel of Fig. 3, we show $D_2(a)$ in G3 (red solid line) and ΛCDM (blue dashed line), with their ratio in the bottom panel, as a function again of the scale factor a. Similarly to D_1, at early times D_2 for G3 and ΛCDM are the same. Moreover, at $a \simeq 0.2$, D_2 in G3 increases much faster than in ΛCDM. The difference is more sizable than in D_1, about 60 per cent for $a = 1$. Since the growth functions are enhanced, cubic Galileon predicts stronger galaxy clustering than ΛCDM. In Fig. 4, we show the ratio of D_2/D_1^2. This ratio is exactly 3/7 in the Einstein–de Sitter universe. The extra clustering power in G3 comes from a larger effective gravitational constant G_{eff} compared to the standard Newton constant G_N.

Figure 4. The ratio D_2/D_1^2 as a function of the scale factor a. The black dotted–dashed line shows the Einstein–de Sitter value of 3/7; while the ΛCDM (blue dashed) line is close to it, the G3 (solid red) deviates substantially.

4 IMPLEMENTATION OF G3 IN PINOCCHIO

The PINOCCHIO code (PINpointing Orbit-Crossing Collapsed Hierarchical Objects; Monaco 1997; Monaco et al. 2002a, b, 2013; Taffoni et al. 2002; Chuang et al. 2015; Munari et al. 2017; Rizzo et al. 2017) is a semi-analytical algorithm for generating realizations of hierarchical formation history of dark matter haloes. It is based on LPT and ellipsoidal collapse. The code evolves the initial linear density field of a given primordial power spectrum on a regular grid in Fourier space. Then, particles are displaced according to Lagrangian PT. For cubic Galileon, the first- and second-order initial displacement fields in Fourier space are given by

$$S_{i,i}^{(1)}(\vec{k}, a_0) = -\delta^{(1)}(\vec{k}, a_0) , \quad (46)$$

$$S_{i,i}^{(2)}(\vec{k}, a_0) = -\frac{1}{2} \int_{\vec{k}_{12}=\vec{k}} \left[1 - \frac{(\vec{k}_1 \cdot \vec{k}_2)^2}{k_1^2 k_2^2} \right] \delta_{k_1}^{(1)}(a_0)\delta_{k_2}^{(1)}(a_0) . \tag{47}$$

The initial time a_0 is arbitrary and related to the normalization choice for the linear power spectrum, PINOCCHIO chooses to normalize at $a_0 = 1$ so that $D_1(a_0) = 1$. For convenience, one can define normalized growth functions

$$D_1'(a) = \frac{D_1(a)}{D_1(a=1)}, \quad D_2'(a) = \frac{D_2(a)}{D_1^2(a=1)} . \tag{48}$$

Then the positions of dark matter particles then are given by

$$\vec{x}(a) = \vec{q} + D_1'(a)\vec{S}^{(1)}(\vec{q}, a_0) + D_2'(a)\vec{S}^{(2)}(\vec{q}, a_0) , \tag{49}$$

where $\vec{S}^{(i)}(\vec{q}, a)$ are the Fourier transforms of the displacements of equation (46).

Ellipsoidal collapse is used to predict the collapsing time of each dark matter particle. The dynamics of ellipsoidal collapse can be completely described by following the evolution of the three principal axes of the ellipsoid (Bond & Myers 1996). The physical length of ellipsoid semi axes is $r_i = a_i q$, where q is the comoving radius of the 'Lagrangian sphere' (a sphere concentric with and sharing the same mass as the ellipsoid, but with density equal to the background density) and a_i denotes the time evolution of each axis. By enforcing mass conservation we can write $a^3 q^3 \bar\rho_{\rm m} = a_1 a_2 a_3 q^3 \rho_{\rm m,e}$, where $\rho_{\rm m,e}$ is the density within the ellipsoid, so that the non-linear overdensity δ is

$$\delta = \frac{a^3}{a_1 a_2 a_3} - 1 . \tag{50}$$

Following the approach of Bond & Myers (1996), we can derive the evolution for the a_i for the G3 model:

$$\frac{d^2 a_i}{dt^2} = \frac{\ddot{a}}{a}a_i - 4\pi G \mu \bar\rho_{\rm m} \left[\frac{\delta}{3} + \frac{5}{4} b_i'(t) + \frac{b_i'(t)}{2}\delta \right] a_i , \tag{51}$$

where

$$b_i'(t) = -\frac{2}{3} + a_1(t)a_2(t)a_3(t)$$
$$\times \int_0^\infty \frac{d\tau}{[a_i^2(t) + \tau]\Pi_{j=1}^3(a_j^2(t) + \tau)^{1/2}} \tag{52}$$

and the deviation from ΛCDM is encoded in the μ function discussed in the previous sections. Equation (51) is an integro-differential equation, which should in principle be solved for each particle, resulting in a computationally expensive prescription. In its standard version, PINOCCHIO relies on an approximation based on LPT to compute collapse times. Such an approximation however does not hold in the case of models where growth is substantially different than ΛCDM. For our purposes, we adopt the description of the ellipsoid's evolution presented in Nadkarni-Ghosh & Singhal (2016). This is equivalent to the Bond & Myers (1996) approach, but avoids the integral of equation (52) by resorting to a set of nine dimensionless parameters:

$$\lambda_{\rm a,i} = 1 - \frac{a_i}{a} , \tag{53}$$

$$\lambda_{\rm v,i} = \frac{1}{H} \frac{\dot{a}_i}{a_i} - 1 , \tag{54}$$

$$\lambda_{\rm d,i} = \frac{\delta}{3} + \frac{5}{4} b_i'(t) + \frac{b_i'(t)}{2}\delta. \tag{55}$$

Here $\lambda_{\rm a,i}$ correspond to the eigenvalues of the deformation tensor and characterize the shape of the ellipsoid, $\lambda_{\rm v,i}$ describe the deviation of the velocity of the ith axis from the background Hubble flow and

$\lambda_{\rm d,i}$ correspond to the eigenvalues of the tensor of second derivatives of the gravitational potential. Taking the time derivative of $\lambda_{\rm a,i}$, $\lambda_{\rm v,i}$, $\lambda_{\rm d,i}$, we obtain the second-order ordinary differential equations

$$\frac{d\lambda_{\rm a,i}}{d \ln a} = -\lambda_{\rm v,i}(1 - \lambda_{\rm a,i}) , \tag{56}$$

$$\frac{d \ln \lambda_{\rm v,i}}{d \ln a} = -\frac{3}{2}\mu\Omega_{\rm m}\lambda_{\rm d,i} - \lambda_{\rm v,i}\left(2 + \frac{\dot{H}}{H^2} \right) - \lambda_{\rm v,i}^2 ,$$

$$\frac{d\lambda_{\rm d,i}}{d \ln a} = -(1 + \delta)\left(\delta + \frac{5}{2} \right)^{-1}\left(\lambda_{\rm d,i} + \frac{5}{6} \right)\sum_{j=1}^3 \lambda_{\rm v,j}$$

$$+ \left(\lambda_{\rm d,i} + \frac{5}{6} \right)\sum_{j=1}^3 (1 + \lambda_{\rm v,j}) - \left(\delta + \frac{5}{2} \right)(1 + \lambda_{\rm v,i})$$

$$+ \sum_{j \neq i} \frac{[\lambda_{\rm d,j} - \lambda_{\rm d,i}][(1 - \lambda_{\rm a,i})^2(1 + \lambda_{\rm v,i}) - (1 - \lambda_{\rm a,j})^2(1 + \lambda_{\rm v,j})]}{(1 - \lambda_{\rm a,i})^2 - (1 - \lambda_{\rm a,j})^2} ,$$

where $\delta = \lambda_{\rm d,1} + \lambda_{\rm d,2} + \lambda_{\rm d,3}$. The initial conditions for this set of equations are

$$\lambda_{\rm a,i} = D_{1,\rm ini}'\lambda_i , \tag{57}$$

$$\lambda_{\rm v,i} = \frac{D_{1,\rm ini}'\lambda_i}{D_{1,\rm ini}'\lambda_i - 1} ,$$

$$\lambda_{\rm d,i} = D_{1,\rm ini}'\lambda_i ,$$

where λ_i is the eigenvalue of $-S_{i,j}^{(1)}(\vec{k}, a_0)$, and $D_{1,\rm ini}'$ is the normalized growth factor D_1' at an initial time $a \sim 10^{-5}$. At this initial time, the Zel'dovich approximation is accurate enough, hence we can compute the 1st-order initial displacement field $S_{i,j}^{(1)}(\vec{k}, a_0)$ from the realization of the density contrast. Then we diagonalize $S_{i,j}^{(1)}(\vec{k}, a_0)$ to get its eigenvalues. Finally, by solving equations (56) we can get the collapse time for each particle. The collapse time is defined as the moment of collapse of the first axis of the ellipsoid collapsed, $\lambda_{\rm a,i} \to 1$.

Collapsed particles may become part of dark matter haloes or of the filament network that connects them. Haloes are constructed with an algorithm that mimics their hierarchical formation: (i) for each collapsing particle the code checks their 6 neighbours in Lagrangian space; (ii) a particle that collapses before its neighbours becomes a 1-particle halo; (iii) a collapsing particle may accrete on a halo if it 'touches' it in Lagrangian space. The accretion condition is satisfied if, after the halo and the particle are moved using equation (49), their distance is less than a threshold distance (discussed below); (v) collapsed particles that do not accrete on haloes become filaments, and may accrete later if a neighbour is accreted to a halo; (vi) halo mergers are checked each time a collapsing particle 'touches' two haloes, the merger takes place if the haloes, moved again with equation (49), get nearer than a threshold distance.

In the PINOCCHIO code, the threshold distance for the collapsed particles being accreted into haloes is defined as

$$d_{\rm thr}^2 = \begin{cases} (f_{\rm a}R^e)^2 + (f_{200}R)^2, & D_1'\sigma \leq \sigma' , \\ \left\{ f_{\rm a}R^e[1 + f_{\rm ra}(D_1'\sigma - \sigma')] \right\}^2 + (f_{200}R)^2, & D_1'\sigma > \sigma' , \end{cases} \tag{58}$$

where $R = (M_{\rm h})^{1/3}$, and $M_{\rm h}$ is the halo mass. The threshold distance for merging between haloes is defined as

$$d_{\rm thr}'^2 = \begin{cases} (f_{\rm m}R_{\rm lar}^e)^2 + (f_{200}R_{\rm lar})^2, & D_1'\sigma \leq \sigma' , \\ \left\{ f_{\rm m}R_{\rm lar}^e[1 + f_{\rm rm}(D_1'\sigma - \sigma')] \right\}^2 + (f_{200}R_{\rm lar})^2, & D_1'\sigma > \sigma', \end{cases} \tag{59}$$

where $R_{\rm lar} = (M_{\rm h,lar})^{1/3}$, with $M_{\rm h,lar}$ is the mass of the larger halo, σ is the variance of the linear density contrast on the grid, and is a function

of time. σ' is a free parameter that controls the change of the 'virial radius', and $\{e, f_a, f_m, f_{ra}, f_{rm}, f_{200}\}$ are additional free parameters that have been calibrated with *N*-body simulation in ΛCDM. Due to the enhancement of gravitational force in G3, the accretion and merging conditions are easier to be satisfied in G3, even for the same halo mass. Via the Poisson equation, one can absorb the gravitational enhancement into the rescaled density and eventually the mass:

$$\frac{\partial^2 \Psi}{a^2} = 4\pi G_{\text{eff}} \delta\rho_{\text{m}} = 4\pi G \delta\rho_{\text{m,eff}} , \qquad (60)$$

where $\delta\rho_{\text{m, eff}} = \mu\delta\rho_{\text{m}}$. The true halo mass is $M_h = \bar{\rho}_{\text{m}} \int_0^{r_{\text{vir}}} 4\pi r^2 \delta\rho_{\text{m}} dr$. After the redefinition, the effective halo mass reads

$$M_{h,\text{eff}} = \bar{\rho}_{\text{m}} \int_0^{r_{\text{vir}}} 4\pi r^2 \delta\rho_{\text{m,eff}} dr = \bar{\rho}_{\text{m}} \int_0^{r_{\text{vir}}} 4\pi r^2 \mu\delta\rho_{\text{m}} dr. \qquad (61)$$

Then one can simply replace the effective masses computed with the above formula in the expression for R and R_{lar}. On linear scales, μ^{L} is independent of radius. From equation (61), one can read $M_{h, \text{eff}} = \mu^{\text{L}}(a)M_h$. On the non-linear scale, $\mu^{\text{NL}}(a, \delta)$ also depends on the radius or equivalently on the local density. For simplification, we fix $\delta = 200$, then $M_{h, \text{eff}} = \mu^{\text{NL}}(a, 200)M_h$. As a consequence, the 5th force is screened in virialized objects. The output halo mass is computed as $N \times m_{\text{p}}$, where N is the number of particles within the halo and $m_{\text{p}} = 4.62 \times 10^9 \, \text{M}_\odot \, h^{-1}$ is the particle mass.

5 RESULTS

We extend the standard PINOCCHIO algorithm according to what described in the previous sections. The code, dubbed as 'G3-PINOCCHIO', will soon be available in the official repository. In order to compare our results with full *N*-body simulations, we choose the box size, number of particles, and cosmological parameters as in Barreira et al. (2013a, 2014a). We run 'G3-PINOCCHIO' in a box with size 200 Mpc h^{-1} with 512^3 particles. The cosmological parameters we adopt are $\Omega_{\text{m}, 0} = 0.279$, $\Omega_{\Lambda 0} = 0.721$, $h = 0.731$, $\sigma_8 = 0.997$, $n_s = 0.953$, both for G3 and ΛCDM. In what follows, we describe three different prescriptions for the G3 model, namely 'linearG3', 'vainG3', and 'grG3'. For all three G3 models, we compute the displacement fields of dark matter particles with 2LPT as presented in Section 3. For 'linearG3', we compute the collapse times with the linear expression for the gravitational slip function, $\mu^{\text{L}}(a)$, with no screening. For 'vainG3', we use the Vainshtein screened gravitational slip function, $\mu^{\text{NL}}(a, \delta)$. In 'grG3' we compute ellipsoidal collapse as in GR: we choose this case as benchmark to demonstrate the effectiveness of the screening mechanism; in fact, the 'grG3' case can be seen as an extreme case of screening. A similar approach is taken in Barreira et al. (2013a, 2014a), where the authors define a 'Linear model', equivalent to our 'linearG3', and a 'Full model', same as our 'vainG3'. However, their 'QCDM model' differs from our 'grG3': the former only modifies the background evolution, while in the latter we modify the 2LPT displacements. As a consequence, our 'grG3' run already includes the power spectrum enhancement predicted by linear theory, i.e. the amplitude of the power spectrum on large scales is the same in 'grG3' and 'linearG3', 'vainG3'.

In Fig. 5, we plot the distribution of collapse times for each particle in a smaller simulation with 200^3 particles and 500 Mpc h^{-1} box size. The upper panel shows the number of collapsed particles for each redshift bin, while the lower panel shows the cumulative numbers. The red, pink, cyan, and purple shaded regions denote, respectively, ΛCDM, 'grG3', 'linearG3', and 'vainG3' models. From the zoom-in sub-panel, we see that at redshift $z = 0$ the cumulative collapsed
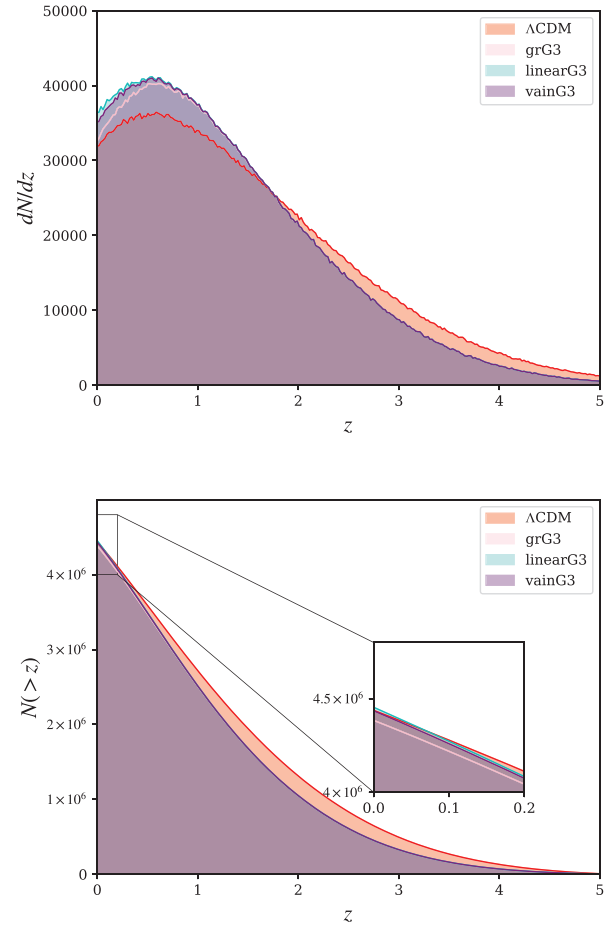

Figure 5. Distribution of collapse times for the dark matter particles (top panel) and its cumulative number (bottom panel) for ΛCDM (red), 'grG3' (pink), 'linearG3' (cyan), and 'vainG3' (purple) as a function of redshift.

particle numbers in ΛCDM and 'vainG3' are almost the same. This is because we normalize the linear power spectra of both ΛCDM and G3 models with the same linear perturbation amplitude at $z = 0$. From the top panel of Fig. 5, one can see that the ΛCDM collapsing rate at low redshift is lower than the one of all G3 models. On the contrary, the ΛCDM model has more collapsed particles above redshift $\sim$1.8. This is because $D'_{1,\text{ini}}$ for ΛCDM is larger than that for G3 by $10 - 15$ per cent (as shown in Fig. 3), thus the ellipsoidal collapse for ΛCDM begins with larger density perturbations. This is again an artefact due to the chosen normalization setup. In the same figure, the 'vainG3' collapsing rate is lower than the one of 'linearG3' between redshifts 0.5 and 0. This is due to the μ^{NL} going back to unity at late times, resulting in a weaker gravitational force with respect to the cases without screening. As an extreme screening limit, 'grG3' further suppresses gravitational collapse.

The input linear power spectrum can be computed with an Einstein–Boltzmann solver such as CAMB/CLASS (Lewis, Challinor & Lasenby 2000; Lesgourgues 2011) or using the analytical fitting formula of Eisenstein & Hu (1998). To suppress sample variance in the power spectrum, the moduli of Fourier-space modes of the linear density field are fixed to their expectation value given by the power spectrum, while phases are randomly distributed between 0 and 2π. Since the linear growth rate in G3 is larger than the one of ΛCDM, to reach the same final amplitude the G3 model has to start from a more uniform density initial condition. For this reason,
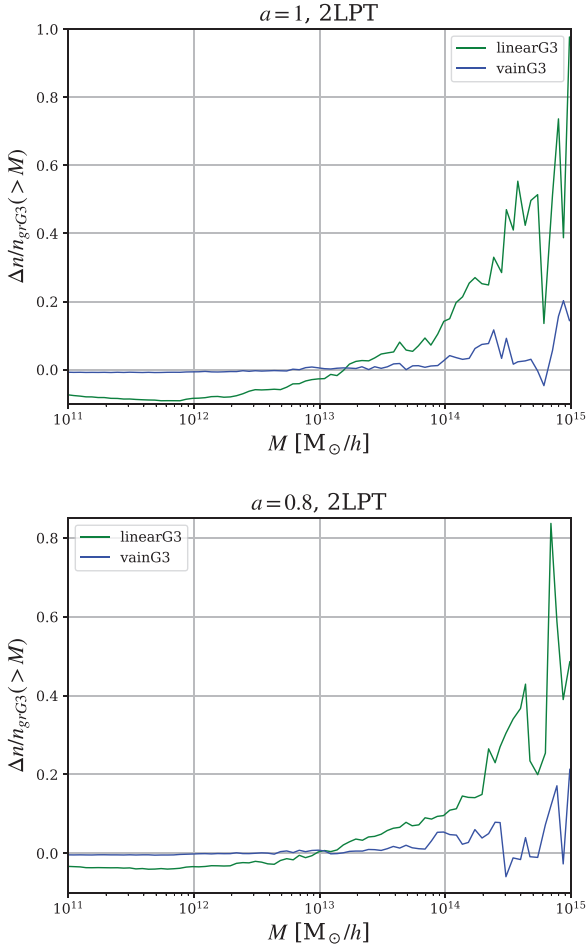
Figure 6. Relative differences in the cumulative mass function with respect to the 'grG3' case at $a = 1$ (top panel) and $a = 0.8$ (bottom panel) for our two approaches to ellipsoidal collapse, 'linearG3' and 'vainG3', shown with green and blue lines, respectively.

Figure 7. Linear halo bias at $a = 1$ (top panel) and $a = 0.8$ (bottom panel), as a function of the halo mass. We mark our predictions with cross symbols, and compare to the results of Barreira et al. (2014a) showing their simulations results with triangles with errorbars, and their prediction based on the Sheth–Tormen formula with solid lines. We show the results for the 'grG3' case, the 'linearG3' case, and the 'vainG3' case with red, green, and blue lines and symbols, respectively.

the high redshift matter power spectra in G3 are lower than those in ΛCDM cases.

In Fig. 6, we show the relative differences in the cumulative mass function of 'linearG3' (green lines) and 'vainG3' (blue lines) with respect to our benchmark, 'grG3'. The role of the Vainshtein mechanism can clearly be seen in the high-mass end, where the fifth force is screened and the 'vainG3' case shows a smaller deviation from 'grG3' than 'linearG3'.

Additionally, we compute the linear halo bias. We use the Pow-erI4 package[8] to read the halo catalogues and compute the halo power spectra at different redshifts, then we compute the square root of the ratio between the halo power spectrum and the linear matter power spectrum for $k < 0.2$, namely the linear halo bias.

In Figure 7 we compare our results for the halo bias with the *N*-body simulations of Barreira et al. (2014a). The cross symbols are our results, the solid curves are the best-fitting Sheth–Tormen formalism to the cumulative halo mass function data from simulations, and the triangles with error bars are the measurement of halo bias directly from the simulations. Different colours mark the different approximations for collapse times, as detailed in the legend. It can be seen that our results, despite being computed with a completely
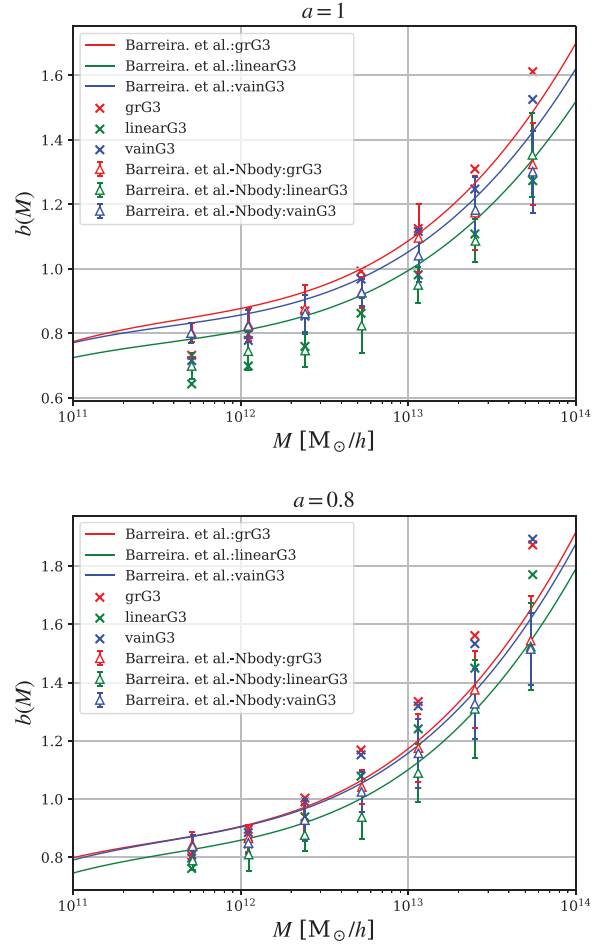
different method, match remarkably well the general trend of the *N*-body simulations.

Finally, we plot our result for the matter power spectrum in Fig. 8. For PINOCCHIO, this is obtained by displacing with 2LPT particles that do not belong to haloes, while halo particles are distributed around the halo centre of mass assuming an NFW profile (Navarro, Frenk & White 1996, 1997). These power spectra are computed with the Pylians package.[9] For comparison, we also show the simulation results with solid curves. The relative differences are with respect to the 'grG3' model in our case, and with respect to the 'QCDM' model in the case of the simulations. One can see that, at large scales, the two results are discrepant: in particular, the Barreira et al. (2013a) ratios also show the amplitude difference in the power spectra that is due to the different linear evolution between G3 and ΛCDM, while ours do not. As mentioned previously, this is due to the fact that our 'grG3' is not exactly the same as 'QCDM', since we modify both the background and the Lagrangian perturbations up to the 2nd order while the 'QCDM' model in Barreira et al. (2013a) only modifies the

[8]https://github.com/sefusatti/PowerI4.

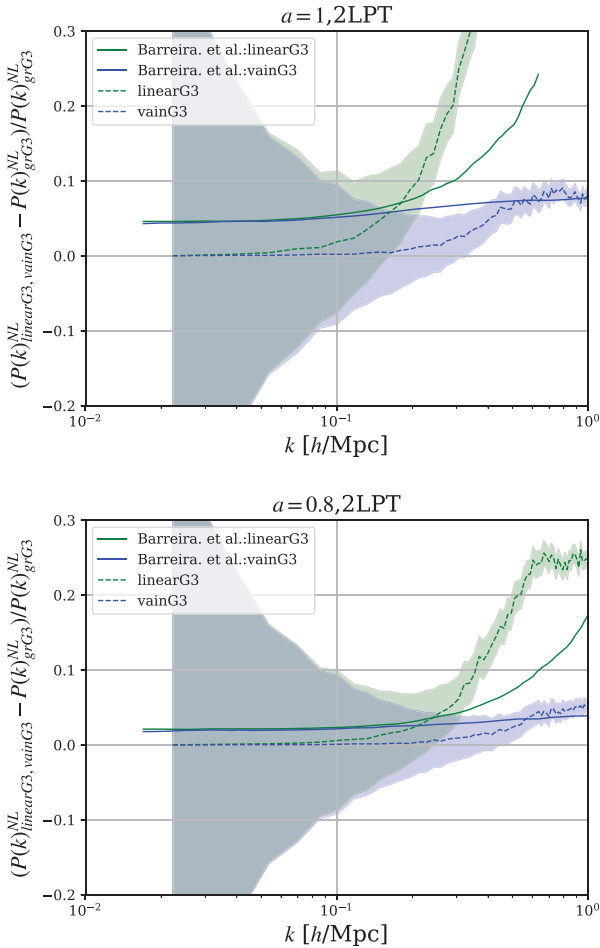[9]https://pylians3.readthedocs.io/en/master/.

Figure 8. Matter power spectrum relative differences at $a = 1$ (top panel) and $a = 0.8$ (bottom panel). The green lines mark the ratio of the 'linearG3' simulations to the 'grG3' case, while we show the 'vainG3' case in blue. Our results, measured from PINOCCHIO snapshots, are plotted as dashed curves. The shadowed areas mark the 1σ errors on the measurements. We also show the results from Barreira et al. (2013a) with solid lines, remarking that these ratios are obtained to their QCDM simulations, which does not correspond to our 'grG3' case exactly since it only includes modifications to the background evolution.

background evolution. For this reason, we cannot do a quantitative comparison with Barreira et al. (2013a), although it can be seen that our results reproduce the general trend of the simulations. We report in Appendix A a more detailed analysis of our halo catalogues. We compare the halo properties of matched and unmatched catalogues, including the halo mass distributions, the halo mass functions, and halo power spectra.

6 CONCLUSIONS

This work presents first- and second-order Lagrangian perturbation theory for the cubic Galileon model, as well as its ellipsoidal collapse dynamics. As in the case of ΛCDM, both the first- and second-order growth factors of the cubic Galileon model are scale independent, since the extra scalar field which drives the accelerated expansion is effectively massless. Its Compton wavelength is indeed on the Hubble horizon scale: below this scale, the modifications of gravity keep constant in space and vary slowly with time. Since both growth functions are larger that their ΛCDM counterparts, as shown in Fig. 3,

clustering in enhanced. In particular, the maximum enhancement of gravity happens at redshift zero, when the effective gravitational constant is about twice the Newton constant. Once we include the Vainshtein screening mechanism in the high local curvature regime, the gravitational interaction restores to the standard GR case.

Using both the extension of standard 2LPT and ellipsoidal collapse to the G3 model, we create a new branch of the PINOCCHIO code, dubbed as G3-PINOCCHIO: our extension provides a fast tool to generate approximated dark matter halo catalogues with the G3 modified gravity model. We run the G3-PINOCCHIO code in a box with size 200 Mpc h^{-1} and 512^3 particles and study the properties of the obtained halo catalogues at different redshifts. To illustrate the effect of Vainshtein screening, we run three different implementations of ellipsoidal collapse, namely 'linearG3', 'vainG3', and 'grG3'. From these realizations, we compute the cumulative mass function, the linear halo bias, and the matter power spectrum. We find that, as for other types of modified gravity, the Vainshtein screening mechanism in cubic Galileon also suppresses the extra gravitational force in the high-mass end of the mass function. We compute the linear halo bias and the matter power spectrum and perform a qualitative comparison to N-body simulations, showing that we can reproduce all trends remarkably well. Given the significantly reduced computational time required to generate halo catalogues with PINOCCHIO with respect to more computationally expensive N-body simulations, our implementation provides an optimal tool for the fast generation of large sets of realizations. Additionally, the code can be readily extended to include other MG models that feature Vainshtein screening.

DATA AVAILABILITY

The data underlying this article will be shared on reasonable request to the corresponding author.

REFERENCES

Abbott B. et al., 2017a, Phys. Rev. Lett., 119, 161101
Abbott B. P. et al., 2017b, ApJ, 848, L13
Aghanim N. et al., 2020, A&A, 641, A6
Alam S. et al., 2017, MNRAS, 470, 2617
Alam S. et al., 2021, JCAP, 11, 050
Amendola L. et al., 2013, Living Rev. Relativ., 16, 6
Babichev E., Deffayet C., Ziour R., 2009, Int. J. Mod. Phys. D, 18, 2147
Baker T., Bellini E., Ferreira P. G., Lagos M., Noller J., Sawicki I., 2017, Phys. Rev. Lett., 119, 251301
Barreira A., Li B., Baugh C. M., Pascoli S., 2012, Phys. Rev. D, 86, 124016
Barreira A., Li B., Hellwing W. A., Baugh C. M., Pascoli S., 2013a, J. Cosmol. Astropart. Phys., 10, 027
Barreira A., Li B., Baugh C. M., Pascoli S., 2013b, J. Cosmol. Astropart. Phys., 11, 056
Barreira A., Li B., Hellwing W. A., Lombriser L., Baugh C. M., Pascoli S., 2014a, J. Cosmol. Astropart. Phys., 04, 029

Barreira A., Li B., Baugh C., Pascoli S., 2014b, J. Cosmol. Astropart. Phys., 08, 059

Barreira A., Bose S., Li B., 2015, J. Cosmol. Astropart. Phys., 2015, 059

Bloomfield J., Flanagan É. É., Park M., Watson S., 2013, J. Cosmol. Astropart. Phys., 2013, 010

Bond J. R., Myers S. T., 1996, ApJS, 103, 1

Bull P. et al., 2016, Phys. Dark Univ., 12, 56

Carroll S. M., 2001, Living Rev. Relativ., 4, 1

Chuang C.-H. et al., 2015, MNRAS, 452, 686

Creminelli P., Vernizzi F., 2017, Phys. Rev. Lett., 119, 251302

DES Collaboration, 2022, Phys.Rev.D, 105, 023520

De Felice A., Tsujikawa S., 2010, Phys. Rev. Lett., 105, 111301

Eisenstein D. J., Hu W., 1998, ApJ, 496, 605

Ezquiaga J. M., Zumalacárregui M., 2017, Phys. Rev. Lett., 119, 251304

Frusciante N., Pace F., 2020, Phys. Dark Univ., 30, 100686

Frusciante N., Perenon L., 2020, Phys. Rep., 857, 1

Frusciante N., Peirone S., Atayde L., De Felice A., 2020, Phys. Rev. D, 101, 064001

Gubitosi G., Piazza F., Vernizzi F., 2013, J. Cosmol. Astropart. Phys., 1302, 032

Hernández-Aguayo C., Arnold C., Li B., Baugh C. M., 2021, MNRAS, 503, 3867

Heymans C. et al., 2021, A&A, 646, A140

Hinterbichler K., Khoury J., 2010, Phys. Rev. Lett., 104, 231301

Hu B., Raveri M., Frusciante N., Silvestri A., 2014, Phys. Rev. D, 89, 103530

Ishak M., 2019, Living Rev. Relativ., 22, 1

Khoury J., Weltman A., 2004, Phys. Rev. Lett., 93, 171104

Koyama K., 2018, Int. J. Mod. Phys. D, 27, 1848001

Lesgourgues J., 2011, preprint(arXiv:1104.2932)

Lewis A., Challinor A., Lasenby A., 2000, ApJ, 538, 473

Li B., Zhao G.-B., Teyssier R., Koyama K., 2012, J. Cosmol. Astropart. Phys., 01, 051

Li B., Zhao G.-B., Koyama K., 2013, J. Cosmol. Astropart. Phys., 05, 023

Llinares C., Mota D. F., Winther H. A., 2014, A&A, 562, A78

Lombriser L., 2016, J. Cosmol. Astropart. Phys., 11, 039

Monaco P., 1997, MNRAS, 287, 753

Monaco P., Theuns T., Taffoni G., 2002a, MNRAS, 331, 587

Monaco P., Theuns T., Taffoni G., Governato F., Quinn T. R., Stadel J., 2002b, ApJ, 564, 8

Monaco P., Sefusatti E., Borgani S., Crocce M., Fosalba P., Sheth R. K., Theuns T., 2013, MNRAS, 433, 2389

Moretti C., Mozzon S., Monaco P., Munari E., Baldi M., 2020, MNRAS, 493, 1153

Munari E., Monaco P., Sefusatti E., Castorina E., Mohammad F. G., Anselmi S., Borgani S., 2017, MNRAS, 465, 4658

Nadkarni-Ghosh S., Singhal A., 2016, MNRAS, 457, 2773

Navarro J. F., Frenk C. S., White S. D. M., 1996, ApJ, 462, 563

Navarro J. F., Frenk C. S., White S. D. M., 1997, ApJ, 490, 493

Neveu J., Ruhlmann-Kleider V., Conley A., Palanque-Delabrouille N., Astier P., Guy J., Babichev E., 2013, A&A, 555, A53

Nicolis A., Rattazzi R., Trincherini E., 2009, Phys. Rev. D, 79, 064036

Peirone S., Frusciante N., Hu B., Raveri M., Silvestri A., 2018, Phys. Rev. D, 97, 063518

Peirone S., Benevento G., Frusciante N., Tsujikawa S., 2019, Phys. Rev. D, 100, 063540

Piazza F., Vernizzi F., 2013, Class. Quantum Gravity, 30, 214007

Pogosian L., Silvestri A., 2016, Phys. Rev. D, 94, 104014

Puchwein E., Baldi M., Springel V., 2013, MNRAS, 436, 348

Renk J., Zumalacárregui M., Montanari F., Barreira A., 2017, J. Cosmol. Astropart. Phys., 10, 020

Rizzo L. A., Villaescusa-Navarro F., Monaco P., Munari E., Borgani S., Castorina E., Sefusatti E., 2017, J. Cosmol. Astropart. Phys., 01, 008

Schmidt F., 2009, Phys. Rev. D, 80, 043001

Song Y., Hu B., 2021, Sci. Sin. Phys. Mech. Astron., 51, 079511

Taffoni G., Monaco P., Theuns T., 2002, MNRAS, 333, 623

Vainshtein A. I., 1972, Phys. Lett. B, 39, 393

Winther H. A. et al., 2015, MNRAS, 454, 4208

Winther H. A., Koyama K., Manera M., Wright B. S., Zhao G.-B., 2017, J. Cosmol. Astropart. Phys., 2017, 006

Zumalacárregui M., Bellini E., Sawicki I., Lesgourgues J., Ferreira P. G., 2017, J. Cosmol. Astropart. Phys., 08, 019

APPENDIX A: HALO CATALOGUES

We describe here a more detailed analysis of the halo catalogues. Since we use the same initial conditions for the different implementations of the modified gravity model, namely 'linearG3' and 'vainG3', we can match the IDs of haloes that are formed in both simulations. We call them 'matched' haloes, while haloes that are only present in one of the two realizations are called 'unmatched'. In Fig. A1 we show the halo number density for the matched and unmatched haloes.

One can see that most haloes appear in both realizations, while only ~ 1 per cent of the haloes in 'linearG3' are unmatched and ~ 10 per cent haloes in the 'vainG3' are unmatched. In Fig. A2, we show the mass distribution of the matched haloes for the 'linearG3' and 'vainG3' prescriptions. Because the modification to the gravitational slip is stronger in the linear case with respect to
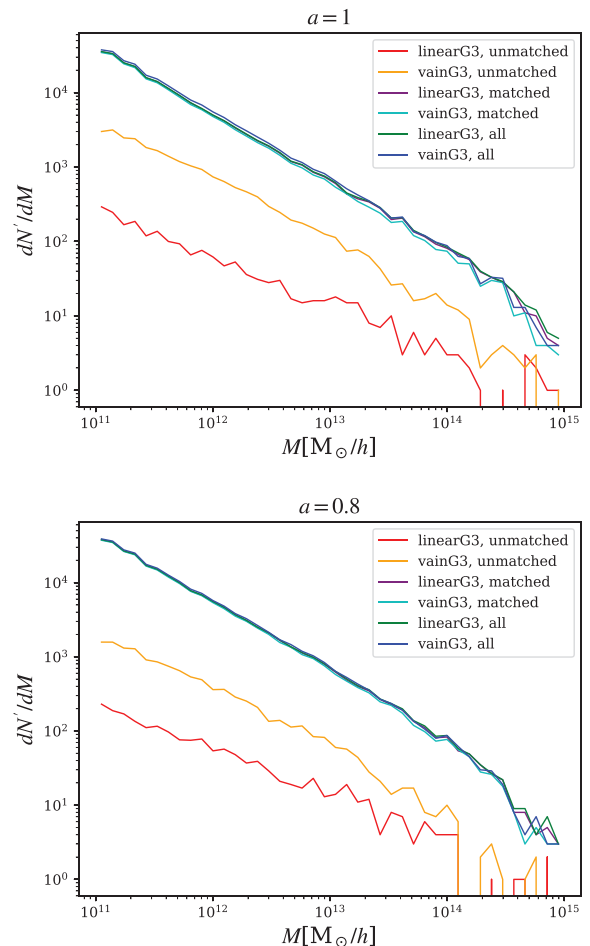

Figure A1. Halo number density dN/dM as a function of the halo mass at $a = 1$ (top panel) and $a = 0.8$ (bottom panel). We show results for the 'linearG3' and 'vainG3' cases, for the whole halo catalogue (marked as *all*, shown with green and blue lines) as well as for the catalogue split in matched (purple and cyan lines) and unmatched (red and orange lines) haloes.
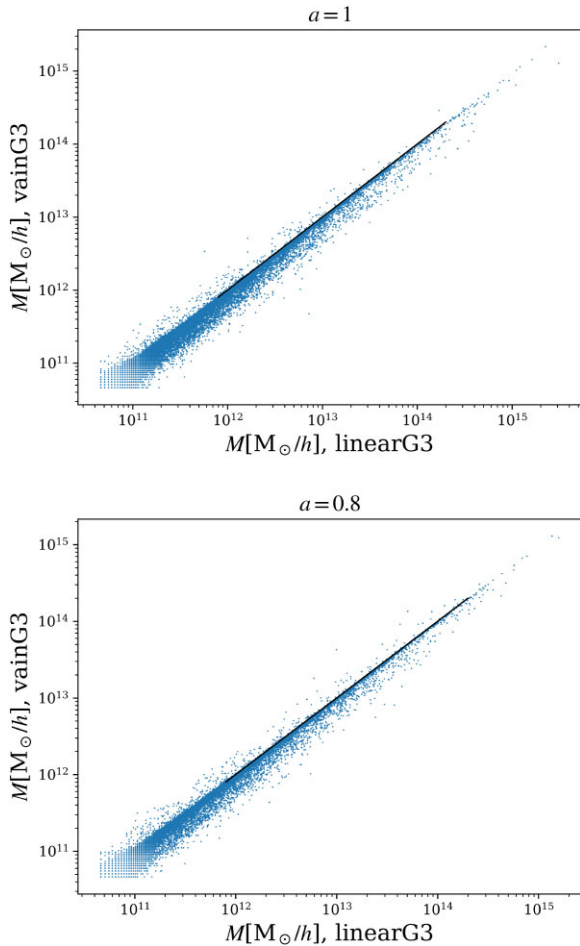
Figure A2. Mass distribution of the matched haloes at $a = 1$ (top panel) and $a = 0.8$ (bottom panel) for the 'linearG3' versus 'vainG3' cases.
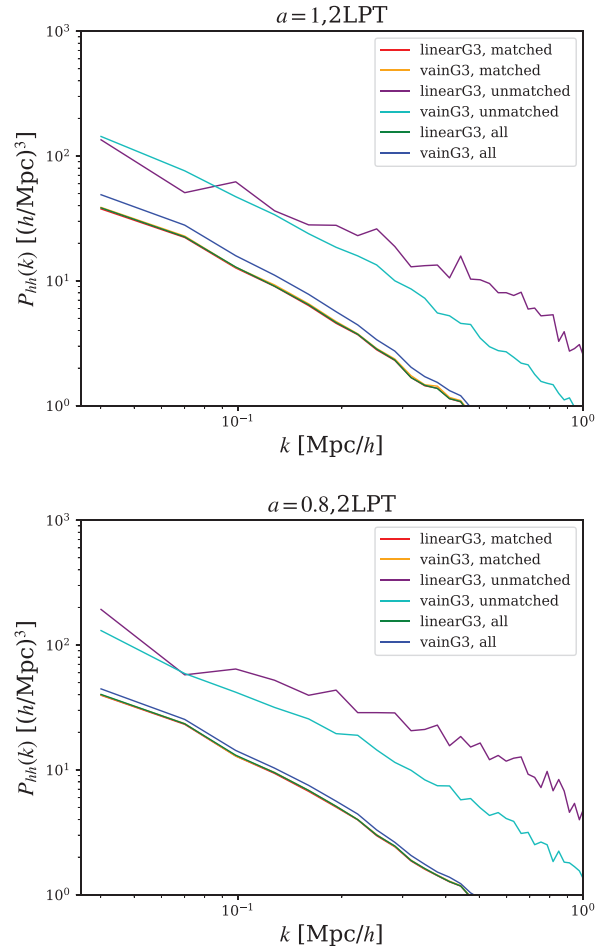

Figure A3. Halo power spectra at $a = 1$ (top panel) and $a = 0.8$. As above, we show results for the whole catalogue, the matched and unmatched haloes.

the non-linear 'vainG3' one, the halo masses shift to the massive direction in the 'linearG3' case (i.e. they mostly sit below the black solid line).

In Fig. A3, we show the halo power spectra computed for the whole catalogue, and for the catalogue split in matched and unmatched haloes. The halo power spectra are computed with PowerI4, considering all haloes with at least 100 particles. It can clearly be seen that the halo power spectra of the matched haloes are very similar for both 'linearG3' and 'vainG3', while they are significantly different for the unmatched haloes. One can conclude that the differences

in the final halo power spectra actually come from the unmatched haloes.

Finally, in Fig. A4 we show the relative differences in the halo power spectra with respect to the 'grG3' model. At $a = 1$, we find a difference of ~ 20 per cent on all scales for 'linearG3'. Such difference is strongly reduced for 'vainG3', highlighting once again the effectiveness of the Vainshtein mechanism in screening the MG fifth force. Similar results can also be seen for $a = 0.8$, with differences of ~ 10 and ~ 2 per cent, respectively, for 'linearG3' and 'vainG3'.
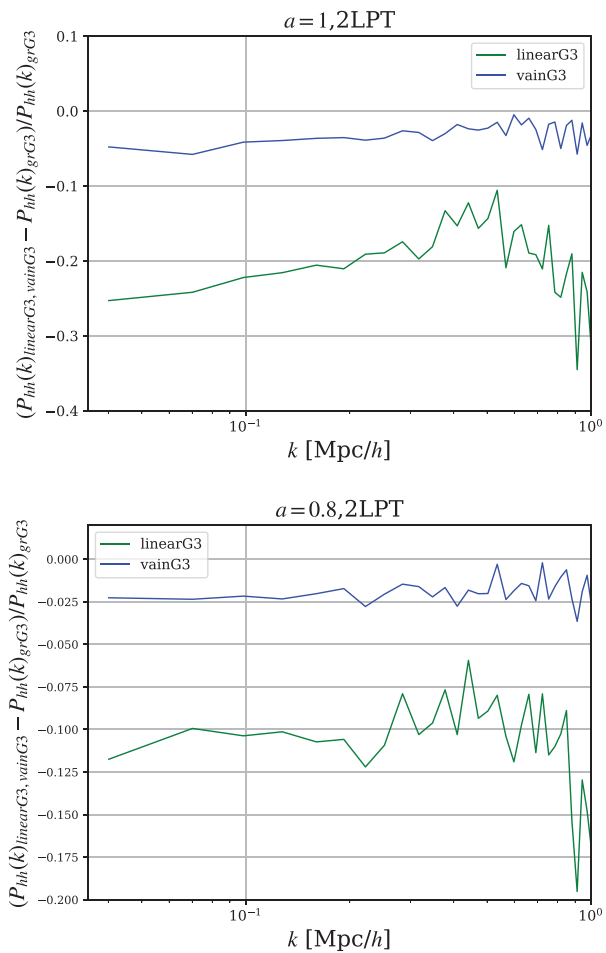
Figure A4. Relative differences in the halo power spectra at $a = 1$ and $a = 0.8$, shown for the 'linearG3' prescription (green line) and the 'vainG3' prescription (blue line). In both cases, the ratio is computed with respect to the 'grG3' case.

This paper has been typeset from a TEX/LATEX file prepared by the author.